Advances in Experimental Medicine and Biology 696

Hamid R. Arabnia
Quoc-Nam Tran *Editors*

Software Tools and Algorithms for Biological Systems

Springer

Advances in Experimental Medicine and Biology

Volume 696

For further volumes:
http://www.springer.com/series/5584

Hamid R. Arabnia • Quoc-Nam Tran
Editors

Software Tools and Algorithms for Biological Systems

Springer

Editors
Hamid R. Arabnia
Department of Computer Science
415 Boyd Graduate Studies
Research Centre
University of Georgia
Athens, GA, USA
hra@cs.uga.edu

Quoc-Nam Tran
Department of Computer Science
Lamar University
Beaumont, TX 77710, USA
qntran@buchberger.cs.lamar.edu

ISSN 0065-2598
ISBN 978-1-4419-7045-9 e-ISBN 978-1-4419-7046-6
DOI 10.1007/978-1-4419-7046-6
Springer New York Dordrecht Heidelberg London

Library of Congress Control Number: 2011921718

Printed on acid-free paper

Springer is part of Springer Science+Business Media (www.springer.com)

Chapter 41
Histopathology Tissue Segmentation by Combining Fuzzy Clustering with Multiphase Vector Level Sets

Filiz Bunyak, Adel Hafiane, and Kannappan Palaniappan

Abstract High resolution, multispectral, and multimodal imagery of tissue biopsies is an indispensable source of information for diagnosis and prognosis of diseases. Automatic extraction of relevant features from these imagery is a valuable assistance for medical experts. A primary step in computational histology is accurate image segmentation to detect the number and spatial distribution of cell nuclei in the tissue, along with segmenting other structures such as lumen and epithelial regions which together make up a gland structure. This chapter presents an automatic segmentation system for histopathology imaging. Spatial constraint fuzzy C-means provides an unsupervised initialization. An active contour algorithm that combines multispectral edge and region informations through a vector multiphase level set framework and Beltrami color metric tensors refines the segmentation. An improved iterative kernel filtering approach detects individual nuclei centers and decomposes densely clustered nuclei structures. The obtained results show high performances for nuclei detection compared to the human annotation.

1 Introduction

Advances in biomedical imaging systems and staining techniques made high resolution, multispectral, and multimodal imagery of tissue biopsies available for diagnosis and prognosis of diseases. But the analysis of these imagery is a subjective, highly tedious, and time-consuming task that requires great expertise. The aim of the newly developing computer-assisted diagnosis (CAD) approaches is to provide new perspectives to develop algorithms for classification of histological images in a clinical setting, to reduce the high variability between analysts caused by subjectivity of the process, and to help processing of increasingly high volumes

F. Bunyak (✉)
Department of Computer Science, University of Missouri-Columbia,
Columbia, MO 65211, USA
e-mail: bunyak@missouri.edu

H.R. Arabnia and Q.-N. Tran (eds.), *Software Tools and Algorithms for Biological Systems*, Advances in Experimental Medicine and Biology 696,
DOI 10.1007/978-1-4419-7046-6_41,

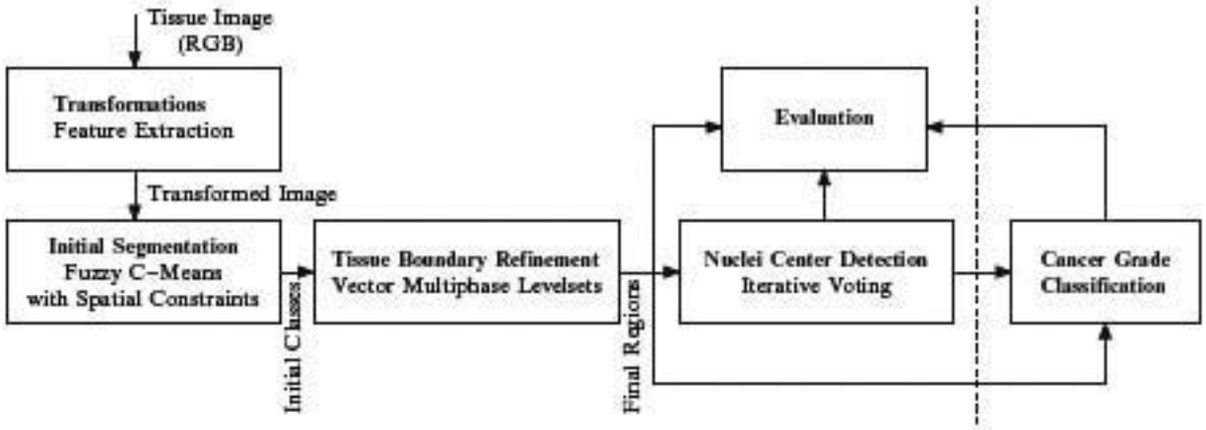

Fig. 1 Process flow for our histopathology image analysis system

of data. Automated quantitative grading of tissue patches is beginning to compare favorably with visual analysis by experts for assigning a Gleason grade to histological imagery. The shape and arrangement of glandular and nuclear structures are related to tissue type. Classification studies use graphs describing the spatial arrangement of the nuclei (i.e., Delaunay triangulation of nuclei centers) [1–6] along with regional intensity and texture features [7–9] to determine tissue type and cancer grade.

This chapter presents a robust image segmentation system for histopathology imagery to be used as a first step to cancer grade classification. The process flow for our histopathology image analysis system is given in Fig. 1. The fuzzy spatial clustering initializes the tissue class, and then the vector-based multiphase level-sets with Beltrami color edge stopping function refine the segmentation. This process allows extraction of nuclei, lumen, and epithelial cytoplasm regions. The detection of individual nuclei centers is performed by an improved iterative voting process. This chapter is extended from our earlier work in [10–12] and is organized as follows. Section 2 describes the fuzzy C-means algorithm with spatial constraint, Sect. 3.1 presents level set-based segmentation refinement process. Section 4 describes nuclei center detection. Results and conclusions are presented in Sects. 5 and 6.

2 Fuzzy C-Means with Spatial Constraint

In this section, we describe the method used to initialize multiclass contours for the multiphase level set image segmentation method. Algorithms based on fuzzy clustering are widely used in color image segmentation. They present good performance in separation of image color classes. It is advantageous to use such kind of methods to initialize level set classes to avoid local minimum convergence and to reduce the number of iterations. The classical fuzzy C-means algorithm is convenient in such cases, but it is not robust to noise, outliers, etc., which could introduce errors in the initialization of level set contours for each class. In [13], we have shown that the spatial correlation reduces noise, outliers, and other artifacts effects. The proposed

spatial constraint for fuzzy C-means (SCFCM) method yields coherent regions and classes. It is based on minimizing the following objective function:

$$J_M(U,V) = \sum_{i=1}^{C}\sum_{j=1}^{N} u_{ij}^m \| \mathbf{x_j} - \mathbf{v_i} \|^2 + \alpha \sum_{i=1}^{C}\sum_{j=1}^{N} u_{ij}^m e^{-\sum_{k\in\Omega} u_{ik}^m} \tag{1}$$

where $X = \{\mathbf{x_1}, \mathbf{x_2}, \ldots, \mathbf{x_N}\}$ denotes the dataset (pixel feature vector). $V = \{\mathbf{v_1}, \mathbf{v_2}, \ldots, \mathbf{v_C}\}$ represents class centers. $U = [u_{ij}]$ is the partition matrix which satisfies the condition: $\sum_i^C u_{ij} = 1 \quad \forall j$, Ω is a set of neighbors. The parameter α is a weight that controls the influence of the second term (spatial information). The objective function (1) has two components. The first component is same as the Fuzzy C-means, the second is a penalty term. This last component reaches the minimum when the membership value of neighbors in a particular cluster is large. Therefore, the classification of a pixel depends strongly on its neighbors membership to a particular class. The optimization of (1) with respect to U was solved using Lagrange multiplier technique. The obtained membership update function is given by:

$$u_{ij} = \frac{1}{\sum_{p=1}^{C} \left(\frac{\|\mathbf{x_j}-\mathbf{v_i}\|^2 + \alpha e^{-\sum_{k\in\Omega} u_{ik}^m}}{\|\mathbf{x_j}-\mathbf{v_p}\|^2 + \alpha e^{-\sum_{k\in\Omega} u_{pk}^m}} \right)^{1/(m-1)}} \tag{2}$$

The method preforms the same steps as the original fuzzy C-means algorithm except for the membership function update.

3 Tissue Boundary Refinement Using Active Contours

While clustering-based algorithms, particularly SCFCM presented in the previous section, provide coarse initial segmentations, further refinement of the tissue boundaries are needed for higher accuracy and robustness. In recent years, PDE-based segmentation methods such as active contours have gained a considerable interest in biomedical image analysis. Active contours evolve a curve $\mathscr{C}$, subject to constraints from a given image. They are classified as parametric [14] or geometric [15, 16] according to their representation. Geometric active contours provide advantages such as eliminating the need to re-parameterize the curve and automatically handling topology changes using a level set implementation [17]. In level set-based active contours, a curve $\mathscr{C}$ is represented implicitly via a Lipschitz function $\phi : \Omega \mapsto \mathbb{R}$ by $\mathscr{C} = \{(x,y) | \phi(x,y) = 0\}$, and the evolution of the curve is given by the zero-level curve of the function $\phi(t,x,y)$ [18]. A regularized Heaviside function is used as a numerical indicator function for the points inside and outside of $\mathscr{C}$. In this section, we present two tissue boundary refinement approaches, a region-based and an edge-based, both using level set-based geometric active contours and both initialized by our SCFCM clustering: (1) vector multiphase active contours, (2) geodesic active contours.

3.1 Region-Based Vector Multiphase Active Contours

In [19], Chan and Vese presented a multiphase extension of their two-phase level set image segmentation algorithm [18]. The multiphase approach enables efficient partitioning of an image into n classes using just $log(n)$ level sets without leaving any gaps or having overlaps between level sets. Chan and Vese also extended their two-phase level set image segmentation algorithm for scalar valued images to vector-valued images such as color or multispectral images [20]. We combine the scalar multiphase approach with the two-phase feature vector approach to handle both multiple image classes and vector-valued imagery. In the case of histopathology imaging derived from H&E-stained cancer tissue biopsies, four image classes have been shown to produce good feature sets for image classification-based cancer grading [3]. We segment multichannel histopathology images using vector multiphase level sets (4-phase in this case) with RGB color as the input feature vector $\mathbf{u_0}$. The two level set functions that partition the image domain Ω into four phases are initialized with four classes obtained from SCFCM, the fuzzy clustering with spatial constraint method, described in Sect. 2. The vector multiphase energy functional $F(\Phi)$ can then be defined as:

$$\begin{aligned} F(\Phi) = \lambda_0 \int_\Omega \| \mathbf{u_0} - \mathbf{c_{00}} \|^2 \, [1-H(\phi_1)][1-H(\phi_2)]\mathrm{d}\mathbf{x} + \lambda_1 \int_\Omega \| \mathbf{u_0} - \mathbf{c_{01}} \|^2 \\ \times [1-H(\phi_1)]H(\phi_2)\, \mathrm{d}\mathbf{x} + \lambda_2 \int_\Omega \| \mathbf{u_0} - \mathbf{c_{10}} \|^2 \\ \times H(\phi_1)[1-H(\phi_2)]\, \mathrm{d}\mathbf{x} + \lambda_3 \int_\Omega \| \mathbf{u_0} - \mathbf{c_{11}} \|^2 \, H(\phi_1)H(\phi_2)\, \mathrm{d}\mathbf{x} \\ + \mu_1 \int_\Omega g(\nabla \mathbf{u_0})\, |\nabla H(\phi_1)| \mathrm{d}\mathbf{x} + \mu_2 \int_\Omega g(\nabla \mathbf{u_0})\, |\nabla H(\phi_2)| \mathrm{d}\mathbf{x} \end{aligned} \tag{3}$$

In order to exploit edge information between different regions, as in [21] for regularization, we use geodesic length measure, $\sum_{1 \le i \le m} \mu_i \int_\Omega g(u_0)|\nabla H(\phi_i)|\mathrm{d}x$ [16], which is basically the length term weighted by an edge stopping function $g(u_0)$. The Euler–Lagrange equations for finding the infimum of 3 can be derived using the calculus of variations as [19]:

$$\begin{aligned} \frac{\partial \phi_1}{\partial t} = \delta(\phi_1) \; \Big\{ \mu_1 \, g(\nabla \mathbf{u_0}) \, \mathrm{div}\left(\frac{\nabla \phi_1}{|\nabla \phi_1|} \right) + \mu_1 \, \nabla g(\nabla \mathbf{u_0}) \cdot \frac{\nabla \phi_1}{|\nabla \phi_1|} \\ - (\lambda_3 \| \mathbf{u_0} - \mathbf{c_{11}} \|^2 - \lambda_1 \| \mathbf{u_0} - \mathbf{c_{01}} \|^2) H(\phi_2) \\ - (\lambda_2 \| \mathbf{u_0} - \mathbf{c_{10}} \|^2 - \lambda_0 \| \mathbf{u_0} - \mathbf{c_{00}} \|^2)[1-H(\phi_2)] \Big\}, \end{aligned}$$

$$\frac{\partial \phi_2}{\partial t} = \delta(\phi_2) \left\{ \mu_2\, g(\nabla \mathbf{u_0})\, \mathrm{div}\left(\frac{\nabla \phi_2}{|\nabla \phi_2|}\right) + \mu_2\, \nabla g(\nabla \mathbf{u_0}) \cdot \frac{\nabla \phi_2}{|\nabla \phi_2|} \right.$$
$$-(\lambda_3 \parallel \mathbf{u_0} - \mathbf{c_{11}} \parallel^2 - \lambda_2 \parallel \mathbf{u_0} - \mathbf{c_{10}} \parallel^2) H(\phi_1)$$
$$\left. -(\lambda_1 \parallel \mathbf{u_0} - \mathbf{c_{01}} \parallel^2 - \lambda_0 \parallel \mathbf{u_0} - \mathbf{c_{00}} \parallel^2)[1 - H(\phi_1)] \right\} \quad (4)$$

where $\mathbf{c_{ij}}$ is the mean feature vector of all pixels associated with class or phase ij, and $\delta(\phi_k) = H'(\phi_k)$ is the Dirac delta function.

3.2 Edge-Based Geodesic Active Contours

In level set-based geodesic active contours [16], the level set function ϕ is evolved using the speed function:

$$\frac{\partial \phi}{\partial t} = g(\nabla \mathbf{u_0})[F_c + \mathscr{K}(\phi)]|\nabla \phi| + \nabla \phi \cdot \nabla g(\nabla \mathbf{u_0}) \quad (5)$$

where F_c is a constant velocity, $\mathscr{K} = \mathrm{div}[\nabla \phi / (|\nabla \phi|)]$ is the curvature term (for regularization), and $g(\mathbf{u_0})$ is an edge stopping function. F_c pushes the curve inward or outward depending on its sign. The regularization term $\mathscr{K}$ ensures boundary smoothness. The external image-dependent force $g(\mathbf{u_0})$ is used to stop the curve evolution at object boundaries. The term $\nabla g \cdot \nabla \phi$ is used to increase the basin of attraction for evolving the curve to the boundaries of the objects.

Although the spatial gradients for single channel images lead to well-defined edge operators, edge detection in multichannel images (i.e., color histopathology images) is not straightforward to generalize since gradients in different channels can have inconsistent orientations. Both in geodesic active contours and in vector multiphase active contours (regularization term in 3), we use an edge stopping function g obtained from Beltrami color metric tensor $\mathscr{E}$ (6) [22] that considers the multichannel image as a vector field and computes the tensor gradient.

$$\mathscr{E} = \begin{bmatrix} 1 + \sum_{i=R,G,B} \left(\frac{\partial \mathbf{I}_i}{\partial x}\right)^2 & \sum_{i=R,G,B} \frac{\partial \mathbf{I}_i}{\partial x} \frac{\partial \mathbf{I}_i}{\partial y} \\ \sum_{i=R,G,B} \frac{\partial \mathbf{I}_i}{\partial x} \frac{\partial \mathbf{I}_i}{\partial y} & 1 + \sum_{i=R,G,B} \left(\frac{\partial \mathbf{I}_i}{\partial y}\right)^2 \end{bmatrix}; \qquad g(\nabla \mathbf{I}) = \exp[-\mathrm{abs}(\mathbf{det}(\mathscr{E})] \quad (6)$$

Classical geodesic active contours are two phase and can segment an image into only two classes. In order to segment the three-class histopathology images, we use two level sets both initialized by SCFCM segmentation mask (Sect. 2). First level set segments the lumen regions from the rest of the image, and second level set

segments the nuclei regions from the rest of the image. Two binary masks one for lumen and one for nuclei classes are produced from the multiclass SCFCM mask (1-for lumen and 0-for everything else, and 1-for nuclei and 0-for everything else, respectively). The masks are dilated with a large enough structuring element to ensure that they fully contain the regions of interests (lumen and nuclei). Geodesic active contours refine the segmentation by moving from the contours of these initial coarse masks inward toward the actual lumen or nuclei boundaries where they stop.

4 Nuclei Center Detection

Segmentation of individual cells or nuclei is an important and challenging necessity for biomedical image analysis. Analysis of cell morphology (shape, structure, color, texture), distribution, motility, and behavior heavily relies on identification of individual cells. In histopathology, image analysis, shape, and arrangement of glandular and nuclear structures are related to tissue type, and graphs describing the spatial arrangement of the nuclei (i.e., Delaunay triangulation of nuclei centers) are used in some automated Gleason grade classification studies [1–3] along with other features. In some tissues, nuclei structures are so densely clustered that staining process cannot visually separate them. In these cases, a cluster separation step is needed for quantification of single nuclei properties. Various approaches have been proposed for cluster decomposition and for individual center or seed point detection in cells and nuclei. These approaches include: watershed segmentation [21,23,24], gradient vector diffusion [25], elliptical model fitting using genetic algorithms [26], regularized centroid transform [27], blob detectors [28], etc. An extensive overview of related work can be found in [29]. Cluster decomposition in histopathology images is particularly challenging because nuclei clusters tend to be tightly fused and large with tens of nuclei.

The module described in this section detects individual nuclei centers from the nuclei mask produced in the previous section. The technique used is based on iterative voting using the oriented kernels approach described in [30, 31]. The approach detects nucleus centers from incomplete boundary information through voting and perceptual grouping. The method applies a series of cone-shaped kernels (Fig. 2a) that vote iteratively along the radial directions [30]. Orientation and shape of the kernel are refined and focused within the iterative process. Center of mass is refined at each iteration until it converges to a focal response. This technique has been chosen because of its noise immunity. Our three additions, such as pre-filtering, improved radial directions, and post-validation, further improve the detection performance.

1. *Pre-filtering* identifies stand-alone nuclei through ellipse fitting. The pre-filtering step have two benefits: (a) by avoiding the unnecessary iterative voting, the nuclei detection process is speeded up; and more importantly, (b) fragmentation (detection of multiple centers for a single nuclei) is considerably reduced. For

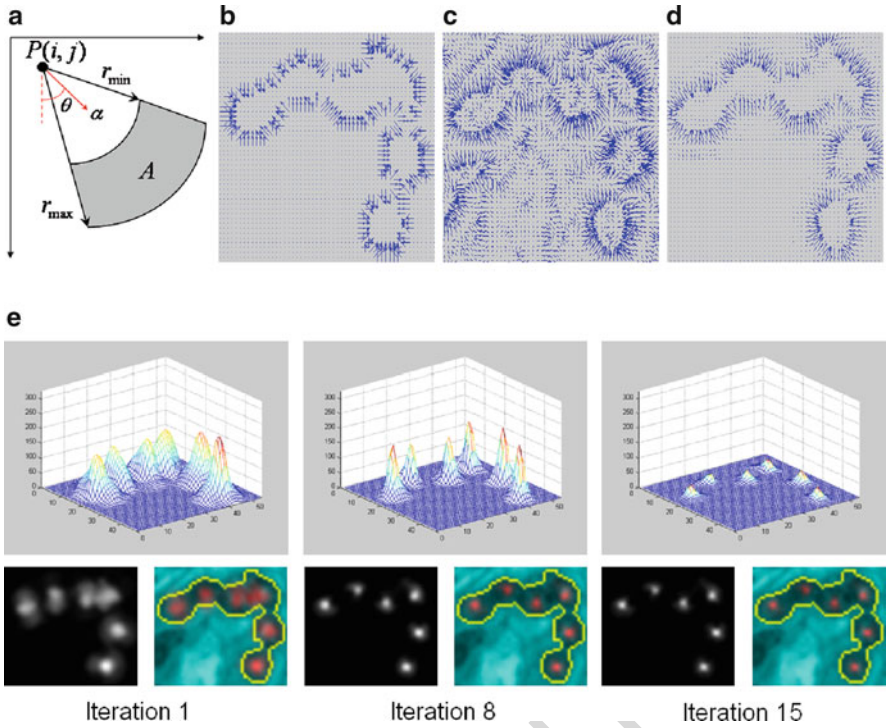

Fig. 2 (**a**) Cone shaped kernel and the voting area. (**b**–**d**) Radial directions: (**a**) from segmentation mask, (**b**) from input image, (**c**) our improved, (**d**) evolution of the voting landscape matrix V during nuclei center detection with iterative voting using improved radial directions in (**d**)

AQ3

this figure will be printed in b/w

elongated ellipses, votes accumulate on multiple peaks rather than a single peak, which results in fragmentation. In histopathology images, stand-alone nuclei tend to be more elongated than the clustered nuclei and produce most of the fragmentation.

2. *Improved radial directions* we incorporate image gradient information and region segmentation information into the computation of radial directions. Use of gradient information contributes to more smooth and precise directions; incorporation of region segmentation information reduces the effects of nuclei and cytoplasm texture. The fusion (Fig. 2d) results in higher precision, better localization, and robustness to cluster contour inaccuracies. Figure 2e shows the evolution of the voting landscape V(i ; j) and the resulting centers for a sample nucleus cluster image.
3. *Post-validation* is a rule-based module that studies each cluster and the associated detected centers, to accept, further split, or merge the centers. The reasoning is done using some statistics on distance between centers, generalized voronoi diagrams, and area of center influence zones.

5 Results and Discussion

The automatic tissue segmentation experiments were evaluated using prostate biopsy histopathology images with various grades of cancer.[1] We applied clustering-based methods [K-means, ~~Fuzzy~~ C-means, and SCFCM (Sect. 2)], active contours segmentation (vector multiphase and geodesic in Sect. 3.1), and their combination.

5.1 Region Segmentation Performance

Figure 3 shows a cropped region from segmentation results of the different techniques on a sample Gleason grade 3 tissue image. K-means and FCM algorithms (shown in Fig. 3b) provide similar results. They do not incorporate any spatial information and tend to fragment regions. The SCFCM method (Fig. 3c) reduces this deficiency using spatial constraints. Both of the level set-based approaches geodesic and vector multiphase (Fig. 3d–f) result in higher segmentation accuracy. For histopathology image segmentation, vector multiphase level sets are more reliable and robust compared to geodesic active contours. Geodesic active contours are

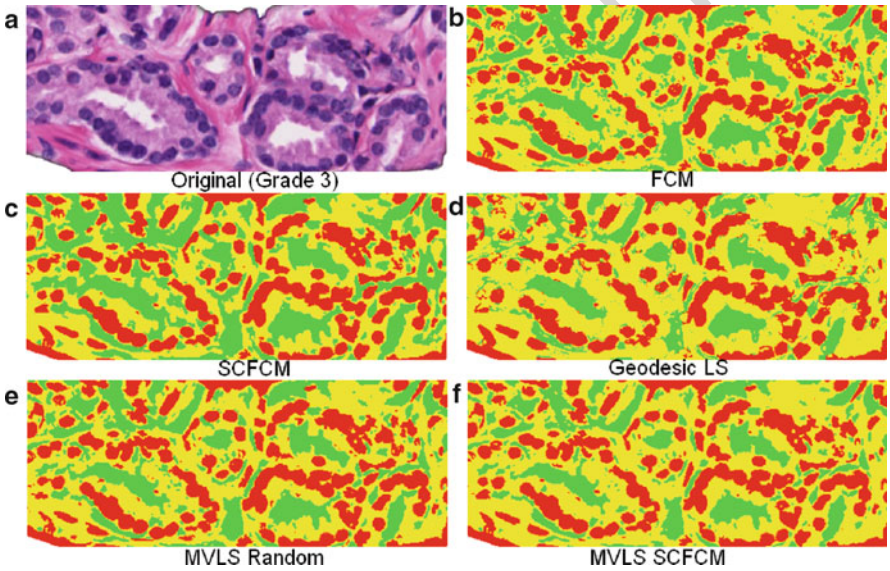

AQ4 **Fig. 3** Automatic segmentation of Gleason grade 3 histopathology image with nuclei shown in *red*, lumen in *green*, epithelial cytoplasm in *yellow*

[1] Histopathology imagery provided by Michael Feldman (Department of Surgical Pathology, University of Pennsylvania) and ground truth from Anant Madabhushi (Rutgers).

Table 1 Region segmentation measures for classes nuclei (C1), lumen (C2), and the cytoplasm (C3). (a) Confusion matrix, (b) M_I,$\mathscr{H}$ criteria

Ground truth	C1 %			C2 %			C3 %				
Segmented	C1	C2	C3	C1	C2	C3	C1	C2	C3	M_I	$\mathscr{H}$
Ground truth	100.0	0.0	0.0	0.0	100.0	0.0	0.0	0.0	100.0	100	100
K-means	74.5	1.2	23.9	0.5	88.9	10.6	8.0	23.7	68.3	68.8	60.3
FCM	74.8	1.2	23.5	0.5	89.2	10.3	8.1	24.3	67.6	68.9	60.08
SCFCM	75.7	2.4	21.9	0.6	92.4	7.0	8.4	35.0	56.6	70.06	63.75
GeodesicSCFCM	74.3	1.8	24.0	0.4	82.0	17.6	10.0	11.7	78.3	78.63	68.05
MVLS-random	77.9	1.1	20.9	0.8	89.3	9.8	10.8	22.0	67.2	73.6	66.35
MVLS-SCFCM	77.8	0.8	21.4	0.6	86.6	12.9	9.0	17.5	73.5	75.9	69.45

more sensitive to initialization (should start either completely inside or outside of the regions of interest). They suffer from contour leaking on weak edges (i.e., some nuclei edges) and early stopping on background edges (i.e., cytoplasm texture). Due to these problems, some significant nuclei regions are missed in Fig. 3d. The vector multiphase level sets (MVLS) are used with two different initialization concepts: uniformly distributed circles and SCFCM segmented regions. As expected, MVLS combined with SCFCM (Fig. 3f) produces better results specially in the lumen regions.

For quantitative region segmentation analysis (Table 1), we used confusion matrix based on the overlap between regions in segmented image and a reference image, and our more detailed evaluation measures *matching index* M_I and $\mathscr{H}$ introduced in [32] that takes into account localization, spatial coherence in terms of position, shape, size, etc., and over- and under-segmentation. While Geodesic-SCFCM results in higher values of M_I, when the over-under segmentation penalty is introduced with $\mathscr{H}$ criterion, MVLS-SCFCM outperforms all the tested methods.

5.2 Nuclei Detection Performance

Our proposed segmentation algorithm, spatial constraint for fuzzy C-means followed by multiphase vector-based level sets (SCFCM + MVLS), is further evaluated using nuclei point set matching. This module compares nucleus center detection results to the ground truth (GT) annotated by the expert. Detected centers are matched to ground truth centers using our automatic correspondence analysis algorithm. This point correspondence algorithm supports not only one-to-one matches but also many-to-one, one-to-many, one-to-none, or none-to-one matches that result from fragmentation, merge (under-segmentation of nuclei clusters), false detection, and missed center, respectively.

Figure 4 shows sample images of the four tissue types and their final SCFCM initiated multiphase vector-based level set segmentation. Merged nuclei regions are further processed to locate individual nuclei centers using the iterative voting (Sect. 4). Table 2 shows nuclei detection performance. Over-segmentation

AQ6

AQ7

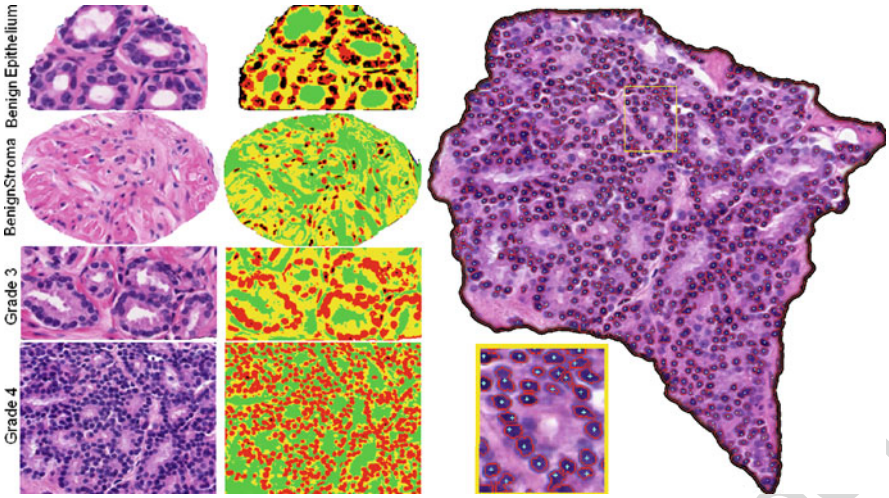

Fig. 4 (**a**) Multiphase vector-based level sets (MVLS) segmentation of four tissue types into three categories: nuclei (*red and black*), lumen (*green*), epithelial cytoplasm (*yellow*). (**b**) Region segmentation and nuclei detection result for a sample Grade 4 image. *Blue*: detected nuclei centers; *red*: nuclei boundaries obtained using marker controlled watershed segmentation. Nuclei center recall: 81%, precision: 96%

this figure will be printed in b/w

t2.1 **Table 2** Statistics of comparison between the automatic nuclei center detection (DT) and the ground truth (GT)

Category	#GT	#DT	#Match (1-to-1)	#Under-segmentation	#Over-segmentation	#False negatives	#False positives	Recall	Precision
Benign epithelium	281	240	194 (69%)	66 (23%)	18 (6%)	3 (1%)	1 (0%)	78%	92%
Benign stroma	286	357	243 (85%)	27 (9%)	13 (5%)	3 (1%)	14 (5%)	90%	72%
Grade 3	553	630	451 (82%)	76 (14%)	15 (3%)	11 (2%)	9 (2%)	87%	77%
Grade 4	1,425	1,282	1,136 (80%)	228 (16%)	55 (4%)	6 (0%)	8 (1%)	85%	95%

(fragmentation) refers to the case where multiple detected centers match to a single ground truth center, under-segmentation (merge) refers to the case where a single detected center corresponds to multiple ground truth centers. False positives correspond to detected center which do not exist in the ground truth. False negative correspond to missed ground truth centers. Table 2 shows an average nuclei recall rate of 85% and an average precision rate of 84% across the four tissue types shown in Fig. 4. It should be noted that the proposed technique works extremely well (in terms of both recall and precision) even for Gleason Grade 4 images (row 4 in Fig. 4) with the highest number and density of cell nuclei. There is also some degree of inconsistency in the quality of the ground truth across experts in identifying indistinct nuclei; thus some of the false positives detected by the algorithm may indeed be correct. Overall, the false negative rate and the false positive rate are less than 5.5% excluding the benign stroma case.

6 Conclusion

In this chapter, we have described a robust fully automatic segmentation system for histopathology imaging derived from H&E-stained cancer tissue biopsies to be used as a first step to cancer grade classification. The system consists of three main modules. Spatial constraint fuzzy C-means developed previously by our group provides an accurate unsupervised initialization. An active contour algorithm that combines multispectral edge and region information through a vector multiphase level set framework and Beltrami color metric tensors refines the region segmentation. The process results in accurate identification of nuclei, lumen, and epithelial cytoplasm regions. Nuclei regions are further processed with an improved iterative kernel filtering approach to detect individual nuclei centers and to decompose densely clustered nuclei structures. Future extensions that we are exploring include incorporating a learning process to accommodate tissue variability as well as using human annotation to improve the overall segmentation accuracy.

References

1. Stotzka, R., Manner, R., Bartels, P., Thompson, D.: A hybrid neural and statistical classifier system for histopathologic grading of prostatic lesions. Analytical and Quantitative Cytology and Histology **17**(3) (1995) 204–218
2. Wetzel, A.: Computational aspects of pathology image classification and retrieval. The Journal of Supercomputing **11**(3) (1997) 279–293
3. Doyle, S., Hwang, M., Shah, K., Madabhushi, A., Feldman, M., Tomaszeweski, J.: Automated grading of prostate cancer using architectural and textural image features. In: IEEE International Symposium Biomedical Imaging: From Nano to Macro ISBI 2007. (April 2007) 1284–1287
4. Wittke, C., Mayer, J., Schweiggert, F.: On the classification of prostate carcinoma with methods from spatial statistics. IEEE Transactions on Information Technology in Biomedicine **11**(4) (2007) 406–414
5. Tabesh, A., Teverovskiy, M., Pang, H., Kumar, V., Verbel, D., Kotsianti, A., Saidi, O.: Multifeature prostate cancer diagnosis and gleason grading of histological images. IEEE Transactions on Medical Imaging **26**(10) (2007) 1366–1378
6. Yang, L., Tuzel, O., Chen, W., Meer, P., Salaru, G., Goodell, L., Foran, D.: PathMiner: A Web-Based tool for Computer-Assisted diagnostics in pathology. IEEE Transactions on Information Technology in Biomedicine **13**(3) (2009) 291–299
7. Huang, P., Lee, C.: Automatic classification for pathological prostate images based on fractal analysis. IEEE Transactions on Medical Imaging **28**(7) (2009) 1037–1050
8. Tosun, A.B., Kandemir, M., Sokmensuer, C., Gunduz-Demir, C.: Object-oriented texture analysis for the unsupervised segmentation of biopsy images for cancer detection. Pattern Recognition **42**(6) (2009) 1104–1112
9. Sertel, O., Kong, J., Catalyurek, U., Lozanski, G., Saltz, J., Gurcan, M.: Histopathological image analysis using Model-Based intermediate representations and color texture: Follicular lymphoma grading. Journal of Signal Processing Systems **55**(1) (April 2009) 169–183
10. Hafiane, A., Bunyak, F., Palaniappan, K.: Fuzzy clustering and active contours for histopathology image segmentation and nuclei detection. Lecture Notes in Computer Science (ACIVS) **5259** (2008) 903–914
11. Hafiane, A., Bunyak, F., Palaniappan, K.: Level-set-based histology image segmentation with region-based comparison. In: MICCAI Workshop on Microscopic Image Analysis with Applications in Biology. (Sep. 2008)

AQ8

12. Hafiane, A., Bunyak, F., Palaniappan, K.: Clustering initiated multiphase active contours and robust separation of nuclei groups for tissue segmentation. In: IEEE International Conference on Pattern Recognition. (2008) Online
13. Hafiane, A., Zavidovique, B., Chaudhuri, S.: A modified fuzzy FCM with Peano scans to image segmentation. In: IEEE International Conference on Image Processing, Genova, Italy (Sept. 2005) 840–843
14. Kass, M., Witkin, A., Terzopoulous, D.: Snakes: Active contour models. International Journal of Computer Vision **1** (1988) 321–331
15. Malladi, R., Sethian, J.A., Vemuri, B.: Shape modelling with front propagation:A level set approach. IEEE Transactions on Pattern Analysis and Machine Intelligence **17**(2) (Feb. 1995) 158–174
16. Caselles, V., Kimmel, R., Sapiro, G.: Geodesic active contours. International Journal of Computer Vision **22**(1) (1997) 61–79
17. Sethian, J.A.: Level Set Methods and Fast Marching Methods: Evolving Interfaces in Computational Geometry, Fluid Mechanics, Computer Vision, and Materials Science. Cambridge University Press, Cambridge, UK (1999) ISBN 0-521-645573-3
18. Chan, T., Vese, L.: Active contours without edges. IEEE Transactions on Image Processing **10**(2) (Feb. 2001) 266–277
19. Vese, L., Chan, T.: A multiphase level set framework for image segmentation using the Mumford and Shah model. International Journal of Computer Vision **50**(3) (2002) 271–293
20. Chan, T., Sandberg, B., Vese, L.: Active contours without edges for vector-valued images. Journal of Visual Communication and Image Representation **11** (2000) 130–141
21. Yan, P., Zhou, X., Shah, M., Wong, S.: Automatic segmentation of high-throughput rnai fluorescent cellular images. IEEE Transactions on Information Technology in Biomedicine **12**(1) (January 2008) 109–117
22. Goldenberg, R., Kimmel, R., Rivlin, E., Rudzsky, M.: Fast geodesic active contours. IEEE Transactions on Image Processing **10**(10) (Oct 2001) 1467–1475
23. Malpica, N., de Solórzano, C., Vaquero, J., Santos, A., Vallcorba, I., Garcia-Sagredo, J., del Pozo, F.: Applying watershed algorithms to the segmentation of clustered nuclei. Cytometry **28**(4) (Aug. 1997) 289–297
24. Ersoy, I., Palaniappan, K.: Multi-feature contour evolution for automatic live cell segmentation in time lapse imagery. In: IEEE Engineering in Medicine and Biology Society (Aug. 2008) 371–374
25. Li, G., Liu, T., Nie, J., Guo, L., Malicki, J., Mara, A., Holley, S., Xia, W., Wong, S.: Detection of blob objects in microscopic zebrafish images based on gradient vector diffusion. Cytometry Part A **71**(10) (Oct 2007) 835–845
26. Yang, F., Jiang, T.: Cell image segmentation with kernel-based dynamic clustering and an ellipsoidal cell shape model. Journal of Biomedical Informatics **34**(2) (2001) 67–73
27. Yang, Q., Parvin, B.: Harmonic cut and regularized centroid transform for localization of subcellular structures. IEEE Transactions on Bio-Medical Engineering **50** (2003) 469–475
28. Byun, J., Verardo, M.R., Sumengen, B., Lewis, G.P., Manjunath, B.S., Fisher, S.K.: Automated tool for the detection of cell nuclei in digital microscopic images: Application to retinal images. Molecular Vision **12** (2006) 949–960

AQ9

29. Schmitt, O., Hasse, M.: Morphological multiscale decomposition of connected regions with emphasis on cell clusters. Computer Vision and Image Understanding (2008) in press
30. Parvin, B., Yang, Q., Han, J., Chang, H., Rydberg, B., Barcellos-Hoff, M.H.: Iterative voting for inference of structural saliency and characterization of subcellular events. IEEE Transactions on Image Processing **16**(3) (March 2007) 615–623
31. Schmitt, O., Hasse, M.: Radial symmetries based decomposition of cell clusters in binary and gray level images. Pattern Recognition **41** (2008) 1905–1923
32. Hafiane, A., Chabrier, S., Rosenberger, C., Laurent, H.: A new supervised evaluation criterion for region based segmentation methods. Lecture Notes in Computer Science (ACIVS) **4678** (2007) 439–448

AUTHOR QUERIES

AQ1. Please check all the figures in this chapter proof and verify whether these are acceptable.
AQ2. Please check whether the running title is appropriate.
AQ3. Part (e) is missing in Fig. 2 caption.
AQ4. Since this figure will be printed in B/W, please change the caption accordingly to match with the figure.
AQ5. The parts (a) and (b) in the caption is not found in the Table 1.
AQ6. Please indicate part labels in Fig. 4
AQ7. Since this figure will be printed in B/W, please change the caption accordingly to match with the figure.
AQ8. Please update the reference [12].
AQ9. Please update the reference [29].